


An optoelectronic synapse based on α - In_2Se_3 with controllable temporal dynamics for multimode and multiscale reservoir computing

Received: 22 July 2021

Accepted: 6 September 2022

Published online: 13 October 2022

 Check for updates

Keqin Liu¹, Teng Zhang¹, Bingjie Dang¹, Lin Bao¹, Liying Xu¹, Caidie Cheng¹, Zhen Yang¹, Ru Huang^{1,2,3}✉ and Yuchao Yang^{1,2,3,4}✉

Neuromorphic computing based on emerging devices could overcome the von Neumann bottleneck—the restriction created by having to transfer data between memory and processing units—and help deliver energy-efficient data processing. The van der Waals semiconductor α -phase indium selenide (α - In_2Se_3) offers ferroelectric, optoelectronic and semiconducting properties and is potentially an ideal substrate for information processing, but its physical properties are not well exploited. Here we report an optoelectronic synapse that is based on α - In_2Se_3 and has controllable temporal dynamics under electrical and optical stimuli. Tight coupling between ferroelectric and optoelectronic processes in the synapse can be used to realize heterosynaptic plasticity, with relaxation timescales that are tunable via light intensity or back-gate voltage. We use the synapses to create a multimode reservoir computing system with adjustable nonlinear transformation and multisensory fusion, which is demonstrated using a multimode handwritten digit-recognition task and a QR code recognition task. We also create a multiscale reservoir computing system via the tunable relaxation timescale of the α - In_2Se_3 synapse, which is tested using a temporal signal prediction task.

Two-dimensional ferroelectric materials have interesting physical properties^{1–3}, miniaturization capabilities^{3–5} and potential applications in memory^{6–8} and neuromorphic computing^{7,9}. The van der Waals semiconductor α -phase indium selenide (α - In_2Se_3) has, in particular, been found to exhibit in-plane and out-of-plane ferroelectricity at room temperature, even when thinned to the monolayer limit^{10–12}. The ferroelectric and semiconducting properties of α - In_2Se_3 mean that it could be of use in a variety of device architectures including ferroelectric

semiconductor junctions (FSJs)^{13–15}, ferroelectric field-effect transistors (FeFETs)¹⁶ and ferroelectric semiconductor field-effect transistors (FeSFETs)^{6,7,9}. In addition, α - In_2Se_3 has a dipole locking effect^{17,18}, which provides a means to manipulate ferroelectric polarization and device characteristics¹³. In_2Se_3 also exhibits excellent optical properties and could be of use in the development of photodetectors^{19–21} and optoelectronic memory²². The existence of ferroelectric, optoelectronic and semiconducting properties in α - In_2Se_3 means that it is an ideal substrate

¹Beijing Advanced Innovation Center for Integrated Circuits, School of Integrated Circuits, Peking University, Beijing, China. ²Center for Brain Inspired Chips, Institute for Artificial Intelligence, Frontiers Science Center for Nano-optoelectronics, Peking University, Beijing, China. ³Center for Brain Inspired Intelligence, Chinese Institute for Brain Research (CIBR), Beijing, China. ⁴Beijing Academy of Artificial Intelligence, Beijing, China.

✉e-mail: ruhuang@pku.edu.cn; yuchaoyang@pku.edu.cn

for information-processing applications, if its physical properties can be adequately exploited²³.

Neuromorphic computing could potentially overcome the von Neumann bottleneck of traditional computers^{24–26}, offering massive parallelism^{27,28} and high energy efficiency^{29–33}. A reservoir computing (RC) system is a type of machine learning platform composed of an untrained recurrent layer (the reservoir) for nonlinear transformation of inputs into high-dimensional space, followed by a readout layer that can be trained to perform classification of high-dimensional states^{34,35}. Hardware implementations of the reservoir are possible using a variety of physical systems, and implementations using memristive devices have, in particular, made notable progress in processing temporal or sequential data, such as spoken-digit recognition^{36–38}, forecasting of chaotic systems^{37,38}, solving second-order nonlinear dynamic tasks³⁹ and real-time neural activity analysis⁴⁰.

A crucial mechanism for a RC system, where the reservoir states are determined by both present inputs and those from the recent past, is a short-term memory effect characterized by a finite timescale. However, RC systems using memristors usually have non-adjustable timescales with a relatively fixed nonlinear transformation function due to difficulties in tuning the relaxation time or physical mechanism of the reservoir, thus limiting its information-processing capacity. Furthermore, existing RC systems are typically dedicated to single-mode signal processing. Simultaneous multimode signal processing in the same reservoir requires a physical mechanism that is tightly coupled and involves direct cross-mode interactions between the signals.

In this Article we report a ferroelectric α - In_2Se_3 -based optoelectronic synapse with a dynamic temporal response that offers multimode and multiscale signal processing. The synapse provides a variety of short-term and long-term plasticity behaviours, which can be modulated by electrical and optical inputs due to the in-plane ferroelectric and optoelectronic properties of α - In_2Se_3 . The tight coupling between the ferroelectric and optoelectronic processes enables heterosynaptic plasticity⁴¹ by using light intensity or the back-gate voltage to modulate the relaxation timescale and other temporal dynamics of the synapse. Using a reservoir physically implemented with α - In_2Se_3 synapses and a simulated readout layer, we create a mixed-signal (multimode) reservoir computing system with tunable dynamics and multisensory fusion. The system is used to perform a multimode handwritten digit-recognition task (based on the Modified National Institute of Standards and Technology (MNIST) database) and a QR code with a 25% added noise recognition task. Based on the back-gate-tunable relaxation time of the α - In_2Se_3 device, multiple-timescale reservoir computing is also achieved and used to solve a multiple superimposed oscillator (MSO) task.

Ferroelectricity of van der Waals α - In_2Se_3

The synaptic device in this study is schematically depicted in Fig. 1a. The α - In_2Se_3 flakes were mechanically exfoliated and transferred onto the substrate, and the morphology and elemental composition of α - In_2Se_3 were confirmed by energy-dispersive X-ray spectroscopy (EDS) mapping (Supplementary Fig. 1a–e). Subsequently, electrode patterns with a source-drain distance of $\sim 1\ \mu\text{m}$ were formed by electron-beam lithography, and Au (80 nm)/Pd (5 nm) electrodes were deposited by electron-beam evaporation followed by a liftoff process to form a Schottky contact with α - In_2Se_3 . The ferroelectricity of α - In_2Se_3 stems from its crystal structure, as shown in Fig. 1b; that is, α - In_2Se_3 consists of a quintuple layer in which the asymmetric position of the central selenium atom breaks the centrosymmetry, leading to spontaneous out-of-plane (OOP) and in-plane (IP) polarizations¹⁰. The unique covalent-bond configuration results in the interlocking of dipoles and stabilization of ferroelectric polarization down to the monolayer limit. Figure 1c presents an atomic-resolution scanning transmission electron microscopy (STEM) high-angle annular dark-field (HAADF) image of α - In_2Se_3 obtained through a C_s -corrected transmission electron microscope, where the inset shows the magnified image overlaid with calculated

results based on the model in Fig. 1b. Five atomic layers stacked in the sequence Se–In–Se–In–Se can be clearly observed, consistent with the crystal model. Owing to asymmetry, the measured vertical distances between the central selenium layer and the two neighbouring indium layers are 2.55 Å and 1.68 Å, in good agreement with the previous study¹⁰. Moreover, the STEM image in Fig. 1c indicates that the α - In_2Se_3 used in this work has the rhombohedral ($R\bar{3}m$) rather than hexagonal ($P6_3/mmc$) structure. A top-view high-resolution transmission electron microscopy (HRTEM) image of α - In_2Se_3 shows that the d -spacing of the plane family is 3.5 Å (Supplementary Fig. 2), which matches well with the (100) plane of α - In_2Se_3 , once again confirming its crystalline structure.

To investigate the ferroelectricity of α - In_2Se_3 , piezoresponse force microscopy (PFM) measurements were carried out on α - In_2Se_3 flakes transferred onto a gold substrate. OOP polarization mapping reveals the existence of ferroelectric domains separated by domain walls in the same flake, as well as the existence of opposite OOP polarizations among different flakes (Supplementary Fig. 3a–i). We have also simultaneously recorded the OOP and IP signals (Fig. 1d), and opposite OOP and IP ferroelectric polarizations can be clearly observed in the flakes shown in Fig. 1d. Notably, there exists an inverse correspondence between IP and OOP polarizations (Fig. 1d), which unambiguously reveals the dipole locking effect^{17,18}. Furthermore, the polarization reversal under an external electric field was also investigated through switching spectroscopy PFM. The PFM amplitude shows a typical butterfly loop (Supplementary Fig. 4a) and a phase contrast of 180° is also observed (Supplementary Fig. 4b), verifying the flipping of ferroelectric polarization under an electric field. Figure 1e illustrates the Raman spectrum of α - In_2Se_3 flakes on a SiO_2 substrate excited by a 532-nm laser. Raman peaks can be identified at $90\ \text{cm}^{-1}$, $103\ \text{cm}^{-1}$, $182\ \text{cm}^{-1}$ and $193\ \text{cm}^{-1}$, which can be attributed to E_2^+ , $A_1(\text{LO} + \text{TO})$, $A_1(\text{LO})$ and $A_1(\text{TO})$ phonon modes of α - In_2Se_3 , respectively^{42,43}. However, the Raman peak located at $\sim 89\ \text{cm}^{-1}$ exists in both rhombohedral and hexagonal α - In_2Se_3 in previous works^{13,17,43–45}, and therefore HRTEM characterization, as shown in Fig. 1c and Supplementary Fig. 2, is necessary to identify the exact stacking sequence (Supplementary Table 1).

Electrical measurements were applied to the two-terminal Au/Pd/ α - In_2Se_3 /Pd/Au device under dark conditions; this exhibits rectifying current–voltage (I – V) characteristics with a pinched hysteresis loop (Fig. 1f), indicating memristive switching behaviour. Owing to the Schottky contacts formed at source and drain electrodes, the device can be modelled as an α - In_2Se_3 channel connecting two back-to-back Schottky junctions, which is dominated by the reversely biased junction. Moreover, the charge transport across the reversely biased Schottky barrier can be described by the thermionic emission, where a linear relationship is expected between $\ln(I)$ and $V^{1/4}$ (Supplementary Note 1). As shown in Supplementary Fig. 5a–h, good linear fits can be achieved for $\ln(I) - V^{1/4}$ in both set and reset processes at various sweeping voltages, in agreement with the thermionic emission process. Importantly, the IP and interlocked OOP polarizations are switched by an IP electric field, causing the change in the band offset between the α - In_2Se_3 channel and the Au/Pd– α - In_2Se_3 interface, which results in the memristive switching behaviour¹⁴ (Supplementary Fig. 6a,b). When the sweeping voltage is increased gradually, a larger hysteresis loop can be observed (Supplementary Fig. 7a). In particular, when consecutive positive or negative sweeping voltages are applied, one can see that the trace of the second sweep does not follow the retrace of the first sweep exactly, but appears between the trace and retrace of the first sweep (Supplementary Fig. 7b,c), which strongly suggests volatile resistive switching in Au/Pd/ α - In_2Se_3 /Pd/Au devices, and thus temporal dynamics.

Synaptic behaviour by electronic and optical stimulation

To verify the temporal dynamics in the devices, transient electrical measurements were performed on the synaptic device by applying a range of stimulus conditions, as depicted schematically in Fig. 2a. Figure 2b

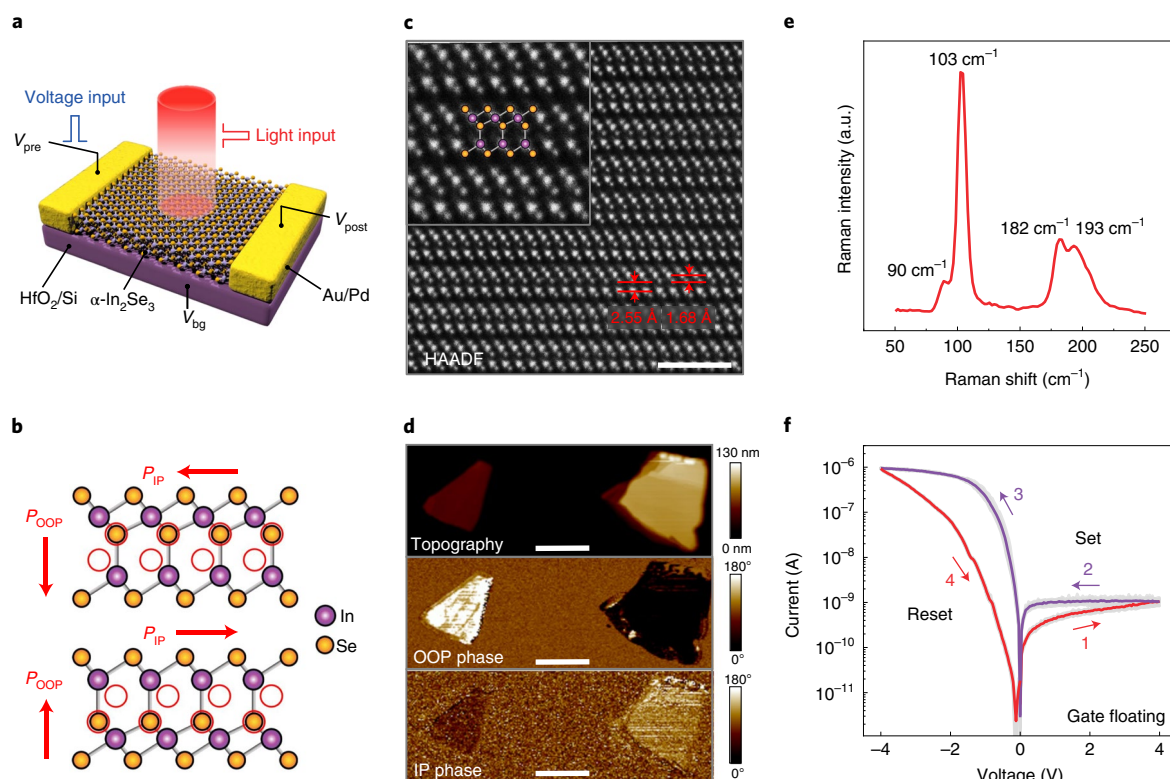


Fig. 1 | Schematic and characterization of ferroelectric van der Waals $\alpha\text{-In}_2\text{Se}_3$. **a**, Schematic of the optoelectronic synapse in this study, with $\alpha\text{-In}_2\text{Se}_3$ as the key function material. **b**, The crystal structure of $\alpha\text{-In}_2\text{Se}_3$, depicting the dipole locking effect. The OOP and IP polarizations are induced by the Se atoms in the central layer, which break the centrosymmetry. The simultaneous OOP and IP polarization reversal is induced by the displacement of central Se atoms towards the bottom-left direction. The orange and purple balls represent Se and In atoms, respectively. **c**, The C_s -corrected STEM-HAADF image of layered

$\alpha\text{-In}_2\text{Se}_3$, demonstrating the layered non-centrosymmetric rhombohedral ($R3m$) structure. Inset: magnified image and corresponding crystal structure. Scale bar, 2 nm. **d**, Topography (top), OOP PFM phase (middle) and IP PFM phase (bottom) images, showing the dipole locking effect in $\alpha\text{-In}_2\text{Se}_3$. Scale bars, 1 μm . **e**, Raman spectrum of $\alpha\text{-In}_2\text{Se}_3$ flakes, with peaks presented at 90 cm^{-1} , 103 cm^{-1} , 182 cm^{-1} and 193 cm^{-1} . **f**, I - V characteristic of the $\alpha\text{-In}_2\text{Se}_3$ device with a pinched hysteresis loop induced by IP ferroelectric polarization switching. The grey lines show the results of ten consecutive I - V sweeps.

shows the current response under positive electrical pulses with increasing amplitude (1, 1.5, 2 and 3 V) but fixed width of 100 ms (the read voltage is +0.1 V). After a positive voltage pulse is applied, it can be seen that the postsynaptic current (PSC) increases abruptly, followed by a rapid decay to its initial state, which mimics the short-term potentiation (STP) effect. Higher pulse amplitude gives rise to a qualitatively similar but more pronounced PSC. Figure 2d also shows the current response under negative electrical pulses with increasing amplitude (−1, −1.5, −2 and −3 V) but fixed width of 100 ms (the read voltage is −0.1 V). When a negative voltage pulse is applied, the PSC rises abruptly upon application of the pulse and subsequently drops to a lower current level than the initial state once the pulse is removed; this is due to the depression effect of the negative pulse. The device, however, gradually decays back to its initial state, which emulates the short-term depression (STD) effect, as shown in Fig. 2d. Similarly, increased amplitude in the negative voltage pulse gives rise to a more prominent depression effect, and the PSC cannot fully recover to the initial state if the voltage amplitude is sufficiently large (for example, −3 V), leading to a transition from STD to long-term depression (LTD). The LTD effect is further demonstrated and observed by applying a sufficiently strong electrical pulse (−4 V, 500 ms), as depicted in Supplementary Fig. 8. In fact, the temporal response of the synaptic device can be inferred from the d.c. result. The application of a negative pulse equates to fast d.c. sweeping from V_{read} to $-V_{\text{max}}$, so the current rises similarly with d.c. sweeping. The end of the negative pulse is equivalent to fast d.c. sweeping from $-V_{\text{max}}$ to V_{read} , and, as a result of the reset process, the current drops to a very low level, which is also consistent with d.c. tests. However, one

should notice the partial switching characteristic that d.c. sweeping exhibits, indicating that the low-current state is volatile and will decay to a higher current level.

To investigate the origin of the short-term memory effect, low-temperature (14 K) measurements were carried out to investigate whether traps or ferroelectric switching of $\alpha\text{-In}_2\text{Se}_3$ contribute to the voltage-induced conductivity decay. The d.c. characteristics of the $\alpha\text{-In}_2\text{Se}_3$ device at 14 K are shown in Supplementary Fig. 9a, where set and reset processes can still be observed. Given that charge trapping/de-trapping is expected to be suppressed at low temperature, the observed memristive switching behaviour should be attributed to ferroelectric polarization switching. On the other hand, the hysteresis loop at 14 K is reduced compared with that at room temperature, which is due to the existence of traps in $\alpha\text{-In}_2\text{Se}_3$. Therefore, traps in $\alpha\text{-In}_2\text{Se}_3$, which are most likely to be surface oxidation states⁴⁶, will contribute to the conductivity decay at room temperature. Supplementary Fig. 9b–d exhibits the dynamic current response when a voltage pulse was applied to three different devices at 14 K. Given that the charge trapping/de-trapping should be suppressed at low temperatures but the conductivity decay can still be observed, the ferroelectric switching may jointly contribute to the conductivity decay. Therefore, both the charge trapping/de-trapping process and ferroelectric switching/relaxation may contribute to the conductivity decay observed in Fig. 2b–e at room temperature. Furthermore, a control experiment was carried out using non-ferroelectric MoS_2 instead of $\alpha\text{-In}_2\text{Se}_3$ to fabricate devices on the same 10-nm atomic layer deposition (ALD)-grown HfO_2/Si substrate. Using the same testing conditions as in Figs. 1f and

2b–e, the d.c. characteristics exhibited negligible hysteresis without memristive switching behaviour, due to the absence of the ferroelectric effect in MoS₂ (Supplementary Fig. 10a). The transfer curve of the MoS₂ transistor shows negligible hysteresis in Supplementary Fig. 10d, once again validating that a limited number of traps exist in the HfO₂ dielectric. Correspondingly, when positive or negative voltage pulses are applied, few transient states can be observed compared with Fig. 2b–g, which proves that the trapping effect in the HfO₂ dielectric is not responsible for the voltage-induced short-term memory effect. The impact of temperature variation on the transient behaviour of the α -In₂Se₃ device was also evaluated from 250 K to 285 K (Supplementary Fig. 11), showing highly consistent transient behaviour with a low coefficient of variation (σ/μ) of 0.14. This level of variation leads to only slight accuracy degradation in network applications (Fig. 5j), implying that α -In₂Se₃ devices can tolerate slight temperature variations without largely affecting the network performance. Moreover, α -In₂Se₃ possesses a relatively high Curie temperature compared with other two-dimensional ferroelectric materials, facilitating high-temperature memory and synaptic applications (Supplementary Note 2).

Based on the above mechanism, a paired-pulse facilitation/depression (PPF/PPD) effect can be achieved by applying a pair of positive/negative pulses to the device. When the second pulse arrives before full relaxation of the PSC induced by the first pulse, the accumulative effect leads to a higher/lower PSC spike, as experimentally shown in Fig. 2c,e. Such a cumulative effect can naturally extend to spike-rate-dependent plasticity. Indeed, when a train of negative pulses (−1 V, 70 ms) with increased frequencies (1, 2, 4 and 8 Hz) were applied to the device, a stronger inhibitory effect could be observed in both the maximum and minimum currents of the spike train, as seen from the linear (middle panel, Fig. 2g) and log scale (bottom panel, Fig. 2g) results. This can be ascribed to the enhanced cumulative effects with smaller time interval, leading to an increased proportion of non-volatile conductance change that cannot recover spontaneously. Figure 2f exhibits the long-term conductance modulation of the α -In₂Se₃ synapse, including both long-term potentiation (LTP) and long-term depression (LTD), by applying a number of identical voltage pulses (where the conductance state is always measured 5 s after pulse application), which corresponds to incremental ferroelectric polarization switching in α -In₂Se₃. The above results unambiguously demonstrate that the α -In₂Se₃-based synaptic device exhibits rich bio-realistic dynamics under various electrical stimuli, making it a promising building block for neuromorphic computing. In particular, the fading memory and nonlinearity of the α -In₂Se₃ devices are of vital importance for the physical implementation of reservoir computing.

Besides the rich temporal dynamics under electrical stimulations, it has been recognized that α -In₂Se₃ has intrinsic optoelectronic properties^{19–22} that are potentially suitable for the implementation of optoelectronic synapses. As schematically depicted in Fig. 3a, the device was illuminated by a 655-nm laser, and a small voltage bias (−0.1 V) was applied to read the device conductance. When the light intensity is increased with a fixed light pulse width of 200 ms, the device exhibits STP with enhanced excitatory PSC (Fig. 3b). This can be ascribed to a light-generated photocurrent that results in a rising of the PSC, followed by a decay process towards the initial state. Detailed fitting and analysis show that the decay curve can be fitted by a double exponential decay function, that is $y = y_0 + y_1 e^{-(x-x_0)/t_1} + y_2 e^{-(x-x_0)/t_2}$, implying the existence of a fast decay mechanism and a slow decay mechanism in the decay process, where $t_1 = 30$ ms and $t_2 = 0.9$ s, taking the rightmost curve in Fig. 3b as an example (Supplementary Fig. 12). In fact, the photocurrent in α -In₂Se₃ can be divided into a fast response caused by an intrinsic photoconduction mechanism and a slow response caused by slow traps¹⁹. With higher light intensity, more photogenerated carriers are produced, so higher current levels can be reached (Fig. 3b), and at the same time a larger number of traps can be filled during this process, leading to a more pronounced slow decay process. Control experiments show that the HfO₂/Si interface makes a negligible current

contribution to the optoelectronic synapse when illuminated with light (Supplementary Fig. 13).

Figure 3c shows the current response under various optical pulse durations with a fixed light intensity of 1.02 mW cm^{−2}. Because the light intensity is unchanged, the intrinsic fast response process reaches a similar level. However, increased illumination time leads to more trap filling, so only the slow decay process is enhanced. The PPF effect can also be achieved by applying a pair of light pulses instead of electrical pulses, as shown in the inset of Fig. 3d, where the PPF ratio $((A_2 - A_1)/A_1)$ increases as the time interval between the paired spikes decreases. This result can be well fitted by a double exponential decay function, as shown in Fig. 3d: PPF ratio = $C_0 + C_1 e^{-\Delta t/t_1} + C_2 e^{-\Delta t/t_2}$. Figure 3e further exhibits the excitatory PSC response when a successive train of optical pulses with varied frequencies are applied to the device. As the spike frequency increases from 1 to 15 Hz, the cumulative effect becomes more pronounced, leading to a higher excitatory PSC response, which is once again qualitatively analogous to the behaviour of electrical synapses. The above light-induced dynamic responses highlight the prospect for in-sensor reservoir computing.

Heterosynaptic plasticity of the α -In₂Se₃ synapse

The results in Figs. 2 and 3 have revealed both electrically and optically stimulated temporal dynamics in the same synaptic device, which are attributed to the ferroelectric and optoelectronic properties of α -In₂Se₃, respectively, therefore providing two degrees of freedom to tune the device dynamics. More importantly, if there are interactions between these two distinct physical processes, the coupling may give rise to more complex synaptic functionalities. Indeed, when light illuminated on the device is considered as a third modulatory terminal while the α -In₂Se₃ synapse is adjusted by electrical stimulations (Fig. 4a), heterosynaptic plasticity can be achieved. That is, when the light intensity is increased from 0 to 1.29 mW cm^{−2}, the overall current levels of the set and reset processes rise dramatically, which can be attributed to the photogenerated carriers, thus reducing the on/off ratio and hysteresis of memristive switching (Fig. 4b). Supplementary Fig. 14a–e further demonstrates the light-tunable dynamic responses of the synaptic device. When a weak electrical pulse (−1.5 V, 100 μ s)/strong electrical pulse (−4 V, 100 ms) was applied to the device illuminated by light with increased intensity, the inhibition effect and relaxation time decrease in agreement with the reduced hysteresis in Fig. 4b, and the overall current level increases due to photocurrent generation. Similarly, the PPD effect is also weakened when the light intensity increases (Supplementary Fig. 14e). Because the time interval between the paired pulses is unchanged, the decreased relaxation time as a result of enhanced light intensity (Supplementary Fig. 14c,d) can lead to a weakened accumulation effect and thus a less pronounced PPD effect (Supplementary Fig. 14e). Inhibitory PSC excited by a successive train of pulses (−1 V, 100-ms pulses with an interval of 50 ms) with varied light intensity once again reveals that the accumulation effect is less pronounced and even vanishes with increased light intensity (Fig. 4d), due to the decreased relaxation time. We have extracted the relaxation time τ of the α -In₂Se₃ synapse under various electrical stimuli and light intensities; this is defined as the duration for the inhibition effect (ΔI) to decay to its 1/e level (Supplementary Fig. 14b). Quantitative analysis reveals that a higher light intensity results in a shorter relaxation time (Fig. 4g), unambiguously verifying that the temporal dynamics of the α -In₂Se₃ synapse can indeed be modulated by the light, making the device capable of working at different timescales.

The existence of a back-gate provides another degree of freedom for tuning the dynamic behaviour, enabling electrically tuned heterosynaptic plasticity. As shown in Fig. 4c, various back-gate voltages were applied during the set and reset processes. When the back-gate voltage was varied from +2 V to −2 V, the overall current level decreased due to the reduced carrier concentration in the n-type In₂Se₃ channel. Furthermore, the hysteresis loop of the reset process shrank, and the

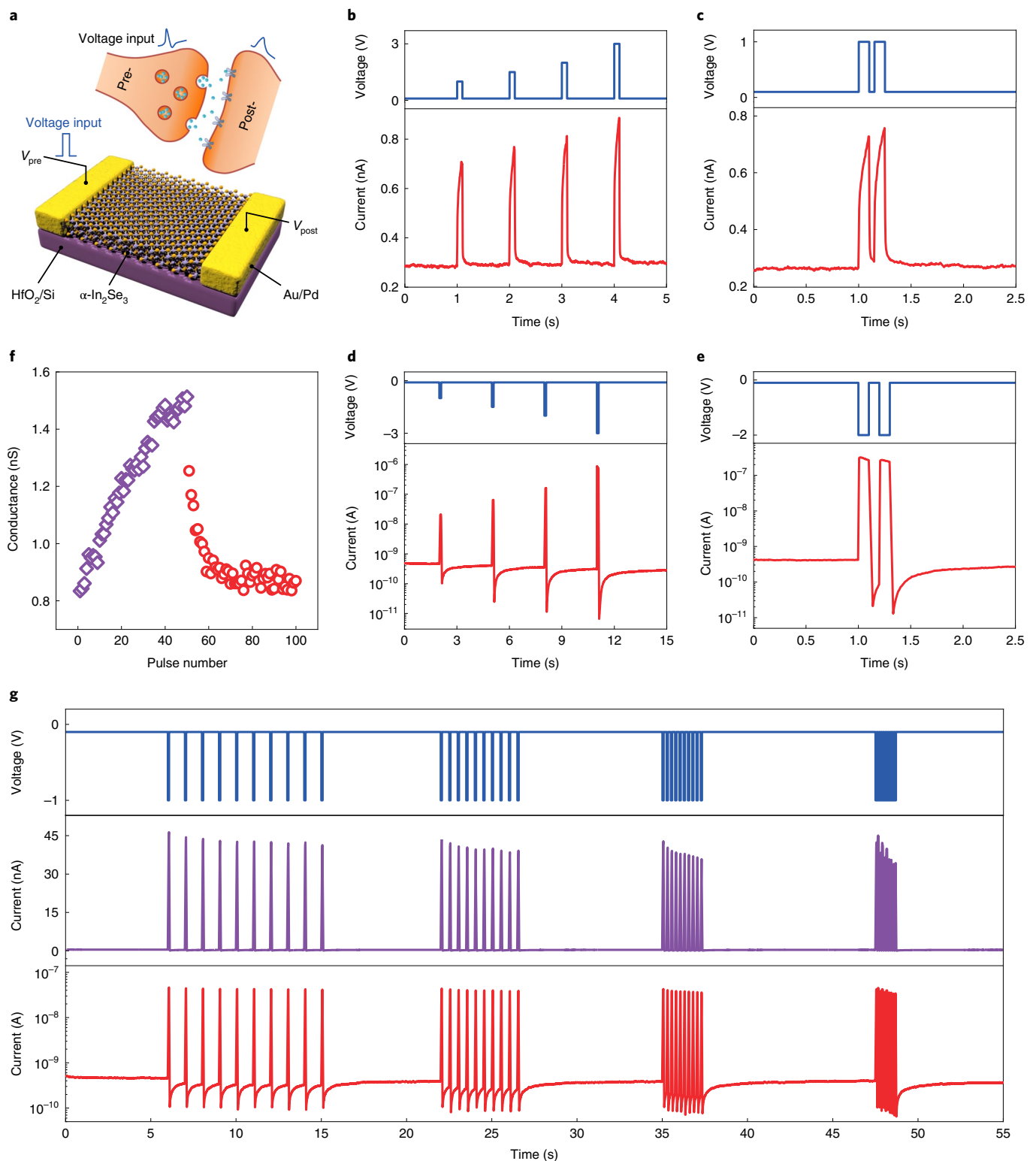


Fig. 2 | Electrical synapse based on ferroelectric $\alpha\text{-In}_2\text{Se}_3$. **a**, Schematic of the electrical synapse and the experimental set-up. **b**, The short-term potentiation effect stimulated by electrical pulses (1, 1.5, 2 and 3 V, 100-ms pulses) with 0.1-V bias to read the device state. **c**, Paired-pulse facilitation effect, where a pair of pulses was applied (1 V, 100 ms, with an interval of 50 ms) with 0.1-V bias to read the device state. **d**, STD effect stimulated by electrical pulses (−1, −1.5, −2 and −3 V, 100-ms pulses) with −0.1-V bias to read the device state. **e**, Paired-

pulse depression effect, where a pair of pulses was applied (−2 V, 100 ms, with an interval of 100 ms) with −0.1-V bias to read the device state. **f**, Long-term potentiation with 50 pulses (2 V, 100 ms) and LTD with 50 pulses (−2 V, 10 ms) with −0.1-V bias to read the device state. **g**, Inhibitory PSC, where a train of pulses was applied (−1 V, 70 ms, with frequencies of 1, 2, 4 and 8 Hz) with −0.1-V bias to read the device state. Higher stimulus frequency leads to a more prominent depression effect.

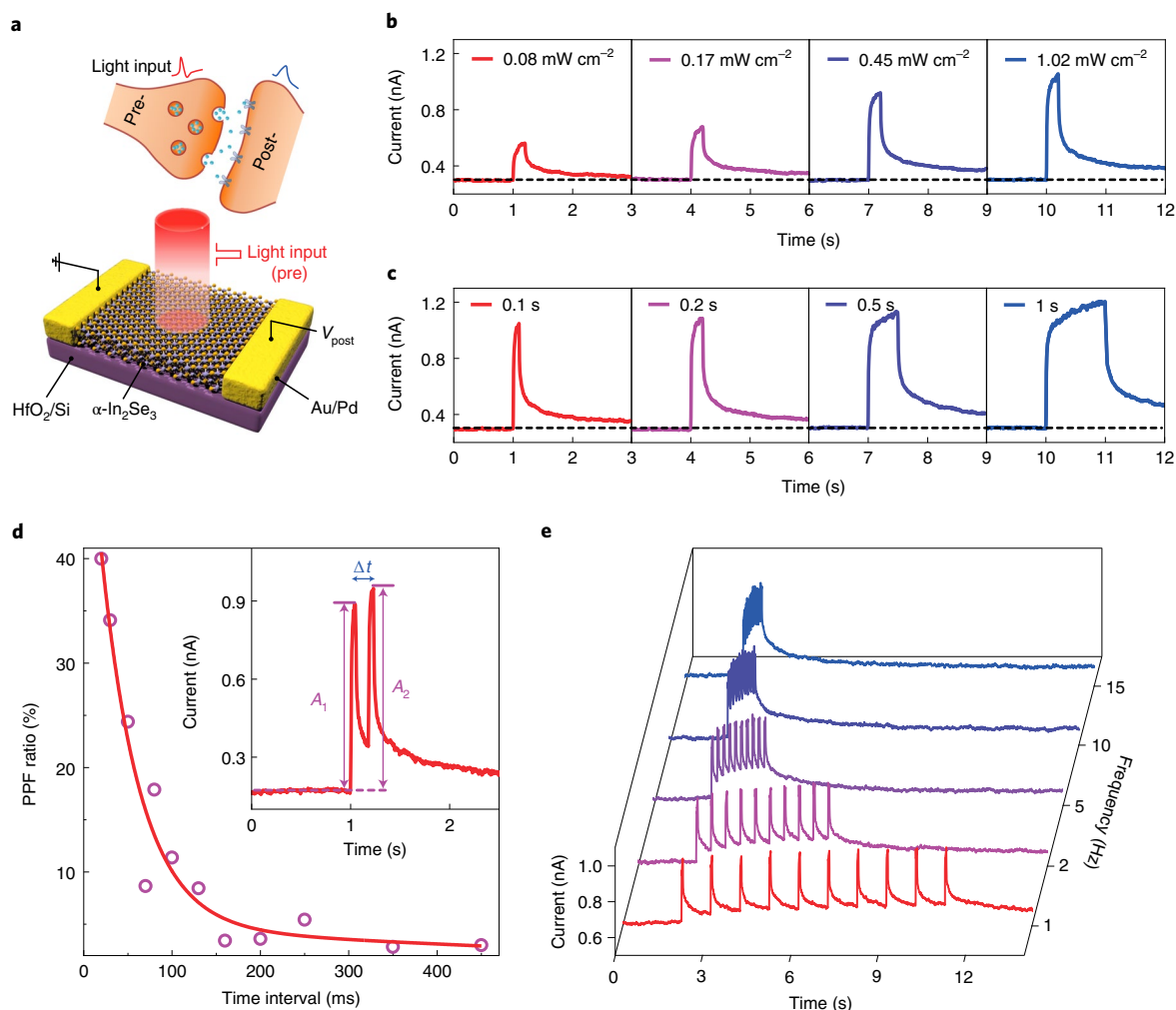


Fig. 3 | Optoelectronic synapse based on the optical response of α - In_2Se_3 . **a**, Schematic of the optoelectronic synapse and experimental set-up. **b**, PSC when optical pulses (0.08 , 0.17 , 0.45 and 1.02 mW cm^{-2} , 200-ms pulses) were applied to the device, exhibiting higher photocurrent with increased light intensity. **c**, PSC when optical pulses with increased illumination time (0.1 , 0.2 , 0.5 and 1 s , 1.02-mW cm^{-2} pulses) were applied to the device; a more prominent slow response caused by slow traps is observed. **d**, PPF ratio as a function of the pulse interval,

defined as $(A_2 - A_1)/A_1 \times 100\%$, where the red line represents fitting results using the double exponential decay function. Inset: the light-induced PPF effect and the definition of A_1 , A_2 and the time interval Δt . **e**, Excitatory PSC induced by a train of optical pulses (1.02 mW cm^{-2} , 50 ms , with frequencies of 1 , 2 , 5 , 10 and 15 Hz) with -0.1-V bias to read the device state, showing that higher pulse frequency leads to a more prominent accumulation effect.

hysteresis loop of the set process enlarged with decreased back-gate voltages. Correspondingly, the transient characteristics can be tuned by the back-gate as well. When a voltage pulse (-2 V , 50 ms) was applied, both the current level and relaxation time gradually decreased as the back-gate voltage was varied from 0 V to -2 V (Fig. 4e). The relaxation time was extracted and is plotted in Fig. 4h, demonstrating that the relaxation time can be shortened by applying negative back-gate voltages. This ability to tune the relaxation time with both light and a back-gate paves the way for multiple-timescale reservoir computing.

The results in Fig. 4b,d have demonstrated that constant light can be employed to modulate the ferroelectric switching process with electrical stimulations. We further studied this physical coupling and interactions when the light is transient and therefore is more meaningful in applications. Figure 4f presents the temporal interactions between a light pulse (1.29 mW cm^{-2} , 50 ms) and a voltage pulse (-2 V , 50 ms), where the timing of the light and voltage inputs was accurately controlled by a pulse generator (Supplementary Fig. 15). If the device is stimulated by a light pulse followed by an electrical pulse with varied time intervals, the light pulse has almost no impact on the subsequent electrical pulse, as shown in Fig. 4i. Since the following voltage pulse is strong enough to cause a full discharge of the trapped

charge carriers responsible for light-induced conductivity decay, this results in the light-induced fading memory being completely erased by the voltage pulse. However, if the device is stimulated by an electrical pulse followed by a light pulse, the photogenerated carriers come into play, while the electrical stimulation-induced relaxation process towards a higher conductance level is still ongoing. As a result, the magnitude of the time interval decides the progress and extension of ongoing conductance relaxation, which in turn determines the detailed conductance state of the α - In_2Se_3 device where the impact of optical pulses is imposed. Therefore, the magnitude of conductance depression increases as the time interval decreases (Fig. 4i), with negligible contribution from conductance relaxation when the electrical and optical pulses are concurrent. This phenomenon clearly verifies the tightly coupled ferroelectric and optoelectronic mechanisms in the device, which provides a vital physical substrate for the processing of optoelectronic signal sequences.

α - In_2Se_3 synapse for multimode signal processing

When artificial neural networks (ANNs) are used to process multimode inputs, the key challenge lies in achieving multisensory fusion. Existing works based on ANNs usually achieve this at the feature level^{47,48}.

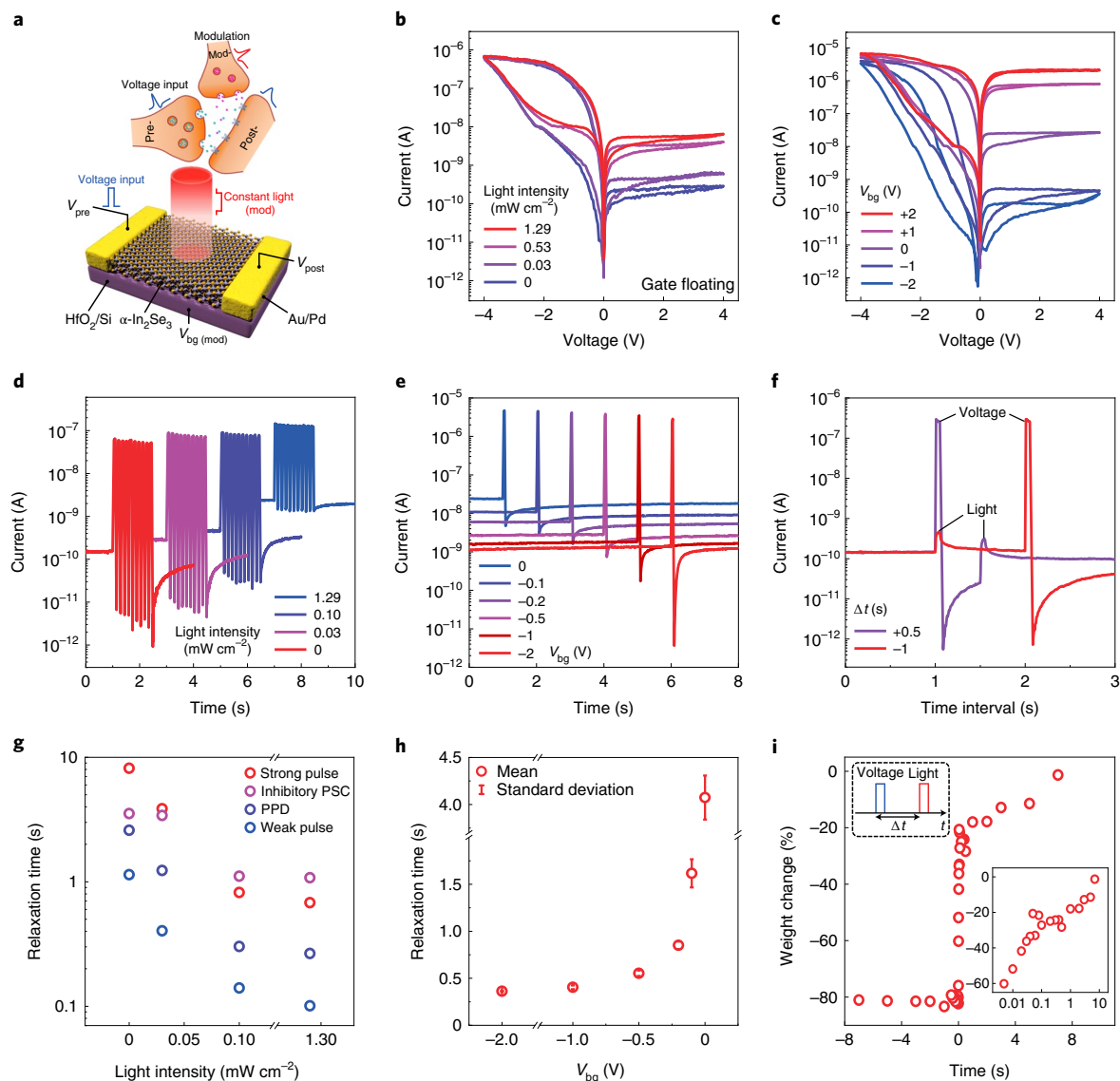


Fig. 4 | Heterosynaptic plasticity of the α -In₂Se₃ device with light/back-gate as modulating terminal. **a**, Schematic of the heterosynapse and the experimental set-up. The two-terminal electrical synapse is modulated by constant light/back-gate as the third terminal. **b**, Switching of the ferroelectric memristor is modulated by constant light (0, 0.03, 0.53 and 1.29 mW cm⁻²), where a higher conduction level and reduced hysteresis loop with increased light intensity are observed. **c**, Switching of the ferroelectric memristor is modulated by the back-gate, where the hysteresis loop of the reset process decreased while the hysteresis loop of the set process increased with the decreased back-gate voltage. **d**, Inhibitory PSC induced by a train of electrical pulses (-1 V, 100 ms, frequency of 6.7 Hz) is weakened by constant light (0, 0.03, 0.10 and 1.29 mW cm⁻²), due to the decreased relaxation time and reduced accumulation effect. **e**, When a voltage pulse (-2 V, 50 ms) was applied with -0.1-V bias, the current level and relaxation time both gradually decreased when the back-gate voltage varied from 0 V to

-2 V. **f**, Two examples of temporal interactions between an electrical pulse (-2 V, 50 ms) and a light pulse (1.29 mW cm⁻², 50 ms) with -0.1-V bias. The time interval (Δt) is defined as $\Delta t = t_{\text{light}} - t_{\text{electrical}}$. **g**, Relaxation time extracted from the results in **d** and Supplementary Fig. 14c-e, which decreases with rising light intensity under various electrical stimuli. In particular, the current reduction with a strong pulse (-4 V, 100 ms) under dark conditions did not recover to its 1/e value within the testing time (8 s). **h**, The relaxation time extracted from **e**, demonstrating that relaxation time can be shortened by applying negative back-gate voltages. **i**, The weight change with different time intervals between the electrical pulse and light pulse, where the current value was acquired 0.5 s after the second pulse. When the time interval is positive, the magnitude of conductance depression increases as the time interval decreases. The positive section of **i** is replotted in the inset, with the time interval shown in logarithmic coordinates.

The input signals are collected by different sensors, and the feature extractions are carried out individually. Afterwards, the extracted features for different modalities are combined together and in turn classified by the classification layer, as shown in Fig. 5a. Accordingly, the feature extraction for each modality can also be carried out by reservoirs individually, where each reservoir responds to one type of input signal (for example, 'EEEE', 'LLLL'), and the features are combined afterwards and classified by the readout layer (Fig. 5b). Notably, if a reservoir can respond to different types of input signal simultaneously,

mixed-input (for example, 'EELL', 'EELL' and 'ELLL') reservoir computing can be realized, where both the feature extractions and multisensory fusion can be achieved within a reservoir (Fig. 5c), therefore enhancing the efficiency.

The mixed-input reservoir discussed above is a generic strategy (mapping approach) for carrying out multisensory fusion within the reservoir computing system, which can be extended to different tasks and different input conditions. A multimode handwritten digit-recognition task based on MNIST is realized (Fig. 5d-j), where

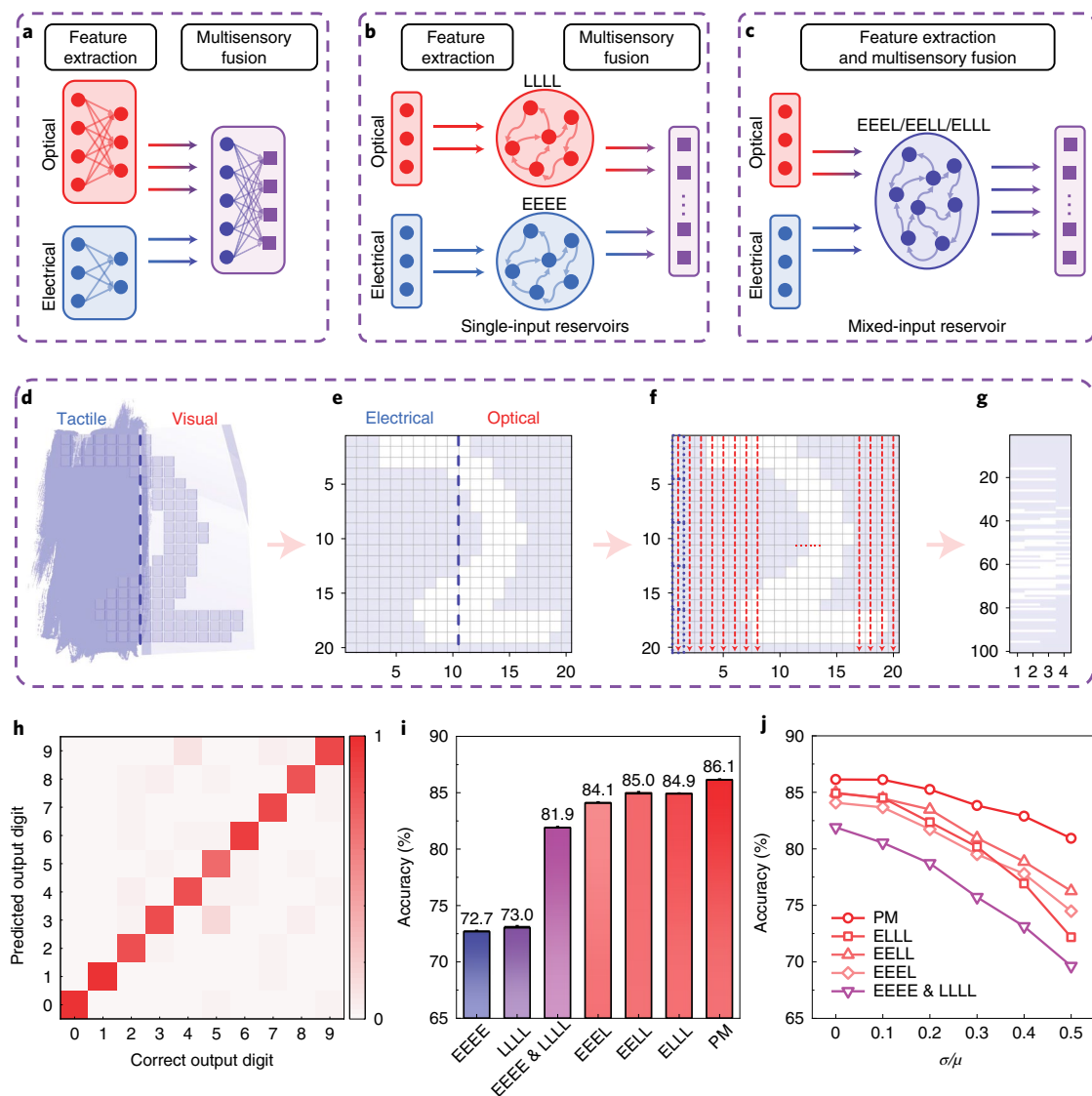


Fig. 5 | Multimode handwritten digit recognition with mixed-input reservoir computing. **a–c.** Schematics of different multisensory fusion architectures. In **a**, feature extraction is carried out for input signals from different sensors individually. Afterwards, the extracted features for different modalities are fused together and classified by the classification layer. In **b**, features from different modalities are extracted by reservoirs individually and fused together for classification. In **c**, feature extraction and multisensory fusion are carried out within a mixed-input reservoir computing system. **d.** Sensing the digit in a complex environment. The left half is covered in paint and can only be sensed by tactile signals, whereas the right half is covered with glass and can only be sensed by visual signals. **e.** The visual input corresponds to optical pulses and the

tactile input corresponds to electrical pulses. **f,g.** The input image (20×20) is grouped into four consecutive pixels vertically (top to bottom) from the leftmost column to the rightmost column and forms a 100×4 input (**f**), where each row is converted into four pulses and applied to the reservoir (**g**). **h.** The confusion matrix for paralleled ‘EEL’, ‘EELL’ and ‘EELL’ modes, where the highest accuracy of 86.1% is achieved. Colour bar: occurrence probability of a given predicted output. **i.** Recognition accuracy of the multimode digit-recognition task for reservoirs working at different modes. **j.** The influence of cycle-to-cycle variation (σ/μ) on network performances, where the recognition accuracy for different modes decreases with increasing σ/μ and PM is most resistant to variation.

inputs from different modalities are partially perceivable. The digit on the left half is covered in paint and can only be sensed via tactile signals, whereas the digit on the right half is covered with glass and can only be sensed via visual signals (Fig. 5d), therefore necessitating multimode inputs and information processing. Because the fabrication of a tactile sensor is outside the scope of this work, we utilized electrical pulses to represent the output signals from a tactile sensor, which can be easily realized by tactile sensors converting pressure to electrical signals (Fig. 5e), so the visual input corresponds to optical pulses and the tactile input to electrical pulses. The input image (20×20) was then grouped into four consecutive pixels vertically (top to bottom) from the leftmost column to the rightmost column, forming a 100×4

input, and each row was converted into four pulses and applied to the reservoir according to the working mode (Fig. 5f,g). For the electrical input, the white pixels in the left half correspond to electrical pulses and the purple pixels to no electrical pulse, whereas all the pixels in the right half correspond to no electrical pulse (Fig. 5e). The opposite is true for the optical input. A schematic for the implementation of the reservoir is presented in Supplementary Fig. 16. In this study, the reservoir can be physically implemented by the α - In_2Se_3 devices. However, the devices are not randomly connected as recurrent connections, because of the difficulties in hardware implementation. Instead, the devices are organized in parallel to process the input voltage signals and generate dynamic output current responses. The current value was

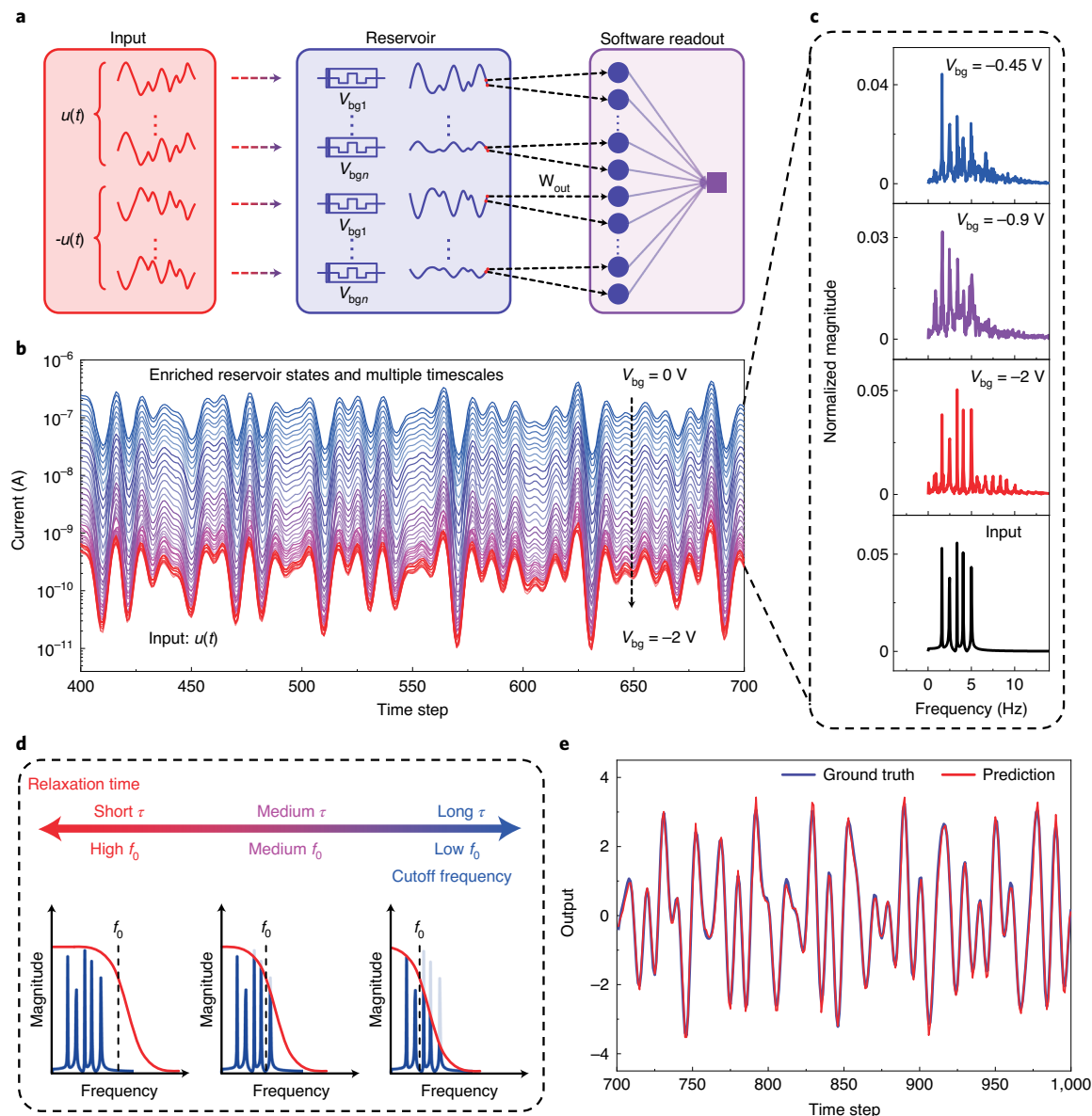


Fig. 6 | Multiple-timescale reservoir computing using memristors with tunable relaxation time. **a**, Schematic of a multiple-timescale RC system. Inputs ($u(t)$ and $-u(t)$) were applied to α -In₂Se₃ devices with varied back-gate voltages (different relaxation times), and the dynamic current responses were collected for readout. **b**, The dynamic current responses of the reservoir, where enriched reservoir states are generated with varied back-gate voltages. **c**, Corresponding FFT results of the current responses in **b**. With less-negative back-gate voltages and longer relaxation time, the α -In₂Se₃ device focuses on slower timescales, with

higher-frequency components gradually suppressed. **d**, Schematic of the low-pass filtering effect with tunable cutoff frequency realized by the α -In₂Se₃ device. The α -In₂Se₃ device with fading memory can perform temporal integration of the input signal, resulting in the low-pass filtering effect. The cutoff frequency is determined by the device relaxation time, which is modulated by the back-gate voltage. **e**, The test results of the MSO₃ task from time steps 701 to 1,000, demonstrating accurate prediction with a normalized root-mean-square error of 0.105.

collected after every four pulses and fed into the software readout layer with ten output neurons (sigmoid activation function) to calculate the probability of different outputs (Supplementary Fig. 16).

When the digit is sent into a single reservoir ('EEEE' or 'LLLL'), part of the digit can be recognized; the left half image can be recognized by 'EEEE' or the right half image by 'LLLL'. With this arrangement, low accuracies of 72.7% or 73.0% are obtained by using 'EEEE' or 'LLLL' alone (Fig. 5i). When carrying out this task with the architecture in Fig. 5b, namely, the whole image is sent into two reservoirs ('EEEE & LLLL') in parallel, information from each half is extracted respectively, then combined for readout. Given the fact that the full information of the digit is extracted, a much higher accuracy of 81.9% is obtained for 'EEEE & LLLL' (Fig. 5i). A mixed-input reservoir (Fig. 5c) can be used to tackle

this problem with different working modes (for example, 'EELL', 'EELL' and 'ELLL'). When the mixed-input reservoir ('EELL') is processing the digit, the 'EE' part responds (the 'LL' part does not respond) to the left half digit and the 'LL' part responds (the 'EE' part does not respond) to the right half. As a result, the full digit can be recognized (with down-sampling in the vertical direction) through the mixed-input reservoir, and further-improved recognition accuracies of 84.1%, 85.0% and 84.9% are realized by the 'EELL', 'EELL' and 'ELLL' modes, respectively (Fig. 5i). Although 'EEEE & LLLL' can extract the full information of the digit, the simultaneous application of two reservoirs on the whole digit doubles the dimensions of the reservoir output. The 'EEEE' reservoir applied to the right half and the 'LLLL' reservoir applied to the left half give no meaningful reservoir outputs, which may interfere with

recognition and result in a lower accuracy than with mixed modes. To further improve the accuracy, the image can be processed by parallel mixed-input (‘PM’) modes ‘EEL’, ‘EELL’ and ‘EELL’, and the highest accuracy of 86.1% can be achieved. The confusion matrix is shown in Fig. 5h. These results unambiguously demonstrate the advantage and importance of using a mixed input rather than a pure electrical/optical input. The effect of cycle-to-cycle variation on recognition accuracy was systematically investigated (Fig. 5j). Measured by the coefficient of variation (σ/μ), the experimental results revealed that the averaged cycle-to-cycle variation of α -In₂Se₃ devices is <0.1 (Supplementary Fig. 17). This level of cycle-to-cycle variation only slightly decreases the recognition accuracy (Fig. 5j) and has a limited impact on PM and other mixed-input reservoir modes (‘EEL’, ‘EELL’ and ‘EELL’).

When the inputs from different modalities are fully perceivable, they can also be successfully fused and processed through the mixed-input reservoir. A noisy QR code recognition task was realized where QR codes were fully perceivable for tactile and visual signals (Supplementary Fig. 18a). QR codes (21 × 21 pixels) representing ten letters from A to J were cut into a slightly smaller size of 20 × 20 pixels and 25% noise was added, as shown in Supplementary Fig. 19a–c. Because QR codes contain information in both the vertical and horizontal directions, they were rotated by two angles (0°, 90°), combined together, and grouped into a 200 × 4 input, where each row was converted into four pulses and applied to the reservoir according to the working mode. An electrical pulse (−2 V, 50 ms) or light pulse (1 mW cm^{−2}, 50 ms) was applied to the device when there was a purple pixel ‘1’. The current value was collected after every four pulses. The readout function is thus a 200 × 10 fully connected network, with ten output neurons (sigmoid activation function) representing the predicted letters A–J (Supplementary Fig. 18a).

The key function of a reservoir is to perform a nonlinear transformation on the input, making it linearly separable in a high-dimensional space. Among the single-input modes (for example, ‘EEEE’ and ‘LLLL’) and mixed-input modes (for example, ‘EEL’ and ‘EELL’), the specific nonlinear transformation and distinguishability of reservoir states may have different effects on solving the problems. The reservoir based on ‘EEEE’ can achieve a recognition accuracy of 89.5%, but the reservoir based on ‘LLLL’ shows better performance, with an accuracy of 97.7%. The nonlinear transformation functions of ‘EEEE’ and ‘LLLL’ are shown in Supplementary Fig. 17a,b,f. The reservoir states of ‘LLLL’ are closely distributed, and the I_{\max}/I_{\min} value of ‘LLLL’ is less than 3. Therefore, as the cycle-to-cycle variation (σ/μ) increases, the overlapping of reservoir states of ‘LLLL’ will increase quickly, resulting in a dramatic degradation in accuracy (Supplementary Fig. 18e). In pursuit of a larger I_{\max}/I_{\min} value and evenly distributed reservoir states, mixed-input modes (‘EEL’ and ‘EELL’) were investigated. The dynamic responses of the reservoir working at ‘EEL’ and ‘EELL’ are demonstrated in Supplementary Figs. 18b and 20, where the optical stimuli utilize the positive dynamic range and the electrical stimuli uses the negative dynamic range, so both dynamic ranges as well as both mechanisms are used, and new transformation relationships are created. As demonstrated in Supplementary Fig. 17c,d, the uniformity of the distribution of reservoir states in ‘EEL’ and ‘EELL’ is improved compared with ‘EEEE’. As a result, performance improvement is achieved by ‘EELL’ (96.3%) compared with ‘EEEE’. Moreover, the recognition accuracy of ‘EELL’ is further improved to 98.6%, which outperforms ‘LLLL’, thanks to the mixed physical mechanism and unique nonlinear transformation. The I_{\max}/I_{\min} values of ‘EEL’ and ‘EELL’ are both more than 10, guaranteeing the tolerance for cycle-to-cycle variation (Supplementary Fig. 18e). The performances of different mixed modes are summarized in Supplementary Fig. 18d. Confusion matrices of ‘EEL’, ‘EEEE’, ‘LLLL’ and ‘EELL’ showing the experimentally obtained classification results from the α -In₂Se₃-based reservoir system versus the correct outputs are shown in Supplementary Fig. 18c (‘EEL’) and Supplementary Fig. 21. To verify the effectiveness of multimode reservoir computing,

a single-valued system was employed for comparison, using the first point of the four pixels as input (Supplementary Note 3). Mode ‘EEL’ outperforms the single-valued network, whereas mode ‘EEEE’ shows lower performance than the single-valued network. Accordingly, the ability to conveniently tune the nonlinear transformation mode and adapt the most suitable nonlinearity for a selected task is important. These results unambiguously demonstrate the advantages of ferroelectric α -In₂Se₃ synapse-based optoelectronic reservoir computing in dynamic multimode signal processing.

α -In₂Se₃ synapse for multiscale signal processing

To extract features more effectively and further enhance computing performance, RC systems operating at multiple timescales are necessary to extract features at various scales^{49–51}. The construction of an RC system working at different timescales, however, requires devices with tunable relaxation times. The relaxation time in conventional short-term devices may only be tuned by controlling the fabrication conditions but is fixed in a particular device. However, the relaxation time of α -In₂Se₃ devices can be tuned easily with light or the back-gate voltage (Fig. 4g,h and Supplementary Fig. 14c–e), exactly meeting the requirement for RC systems operating at different timescales.

Based on the tunable relaxation time of α -In₂Se₃ devices, a MSO task^{52,53} was thus investigated to demonstrate multiple-timescale reservoir computing. The MSO_k time-series data were generated by the summation of sinusoidal functions using the equation

$$u(t) = \sum_{i=1}^k \sin(\varphi_i t), \quad (1)$$

where k denotes the number of sinusoidal functions, φ_i denotes the frequency of the i th sinusoidal function, and t denotes the time step. In this work, the MSO₅ task was carried out and the coefficients φ_i were set as follows⁵³: $\varphi_1 = 0.2$, $\varphi_2 = 0.311$, $\varphi_3 = 0.42$, $\varphi_4 = 0.51$ and $\varphi_5 = 0.63$. Five different frequencies are present in MSO₅, indicating the existence of multiple timescales in this time series. A reservoir that can capture features from multiple timescales is therefore necessary to carry out this task. The relaxation times of α -In₂Se₃ devices can be tuned by applying constant light or a back-gate voltage (Fig. 4). Thus, a reservoir with the capability of processing multiple timescales is proposed by using memristors with different relaxation times, achieved by applying various back-gate voltages (Fig. 6a). The MSO₅ task consists of 1,000 time steps; time steps from 1 to 100 were used for washout, 101 to 700 for training and 701 to 1,000 for testing. The generated time series $u(t)$ and $-u(t)$ were linearly mapped to an appropriate voltage range (−1 V, −0.5 V), and the time interval between each time step was set as 20 ms. Then, two types of input ($u(t)$ and $-u(t)$) were applied to α -In₂Se₃ devices with varied back-gate voltages. The dynamic current responses are shown in Fig. 6b and Supplementary Fig. 22. Fast Fourier transformation (FFT) was carried out in Fig. 6c based on the input of MSO₅ and the current responses of the reservoir. The bottom panel presents the FFT of the input signal, with the five peaks corresponding to five different frequencies. In the case of lower negative back-gate voltages ($V_{bg} = -0.9$ V and $V_{bg} = -0.45$ V) and longer relaxation times, higher-frequency components were gradually suppressed (middle and upper panels, Fig. 6c).

Overall, the α -In₂Se₃ device with fading memory property exhibits a low-pass filtering effect (Fig. 6d). When the frequency of the input signal is higher than the cutoff frequency (f_0) of the α -In₂Se₃ device, such that the input timescale is shorter than the relaxation time (τ) of the device, the fading memory property performs temporal integration over the input signal, so that the high-frequency components are integrated into a relatively low-frequency wave package. If the input timescale is longer than the relaxation time of the α -In₂Se₃ device, the integration will not occur and the input signal can pass through the

α -In₂Se₃ device with harmonic generation due to the nonlinearity of the device. The α -In₂Se₃ device thus exhibits a low-pass filtering effect with cutoff frequency determined by the relaxation time of the device. Moreover, the relaxation time of the α -In₂Se₃ device can be gradually tuned by applying a back-gate voltage, meaning that the cutoff frequency can be adjusted with varied back-gate voltages (Fig. 6d). When a negative back-gate voltage ($V_{bg} = -2$ V) is applied, the cutoff frequency is high enough for all five frequencies to pass the filter with little harmonic generation effect. When the magnitude of the negative back-gate voltages is decreased ($V_{bg} = -0.9$ V and $V_{bg} = -0.45$ V), the cutoff frequency decreases and the high-frequency components of the input are filtered and low-frequency components become dominant (Fig. 6c).

The richness of the reservoir states also has an important influence on the performance of reservoir computing systems. Device-to-device variation can serve as a physical source to produce qualitatively similar, but quantitatively different, current responses, giving rise to enriched reservoir states³⁷. The existence of device-to-device variation is common in memristive devices, as verified in Supplementary Fig. 23, but that approach lacks controllability. Here we propose using varied back-gate voltages to control the carrier concentration (current level) so as to generate rich reservoir states in a highly controllable manner (Fig. 6b). The application of back-gate voltages has thus led to two advantages simultaneously: multiple-timescale representation and enriched reservoir states. After applying two types of input ($u(t)$ and $-u(t)$) to the reservoir, the current responses were collected from the memristor with n types of back-gate voltage (to achieve multiple timescales), with the back-gate voltages varying from 0 V to -2 V in -0.1 -V steps ($n = 21$ for this task). One-step-ahead prediction was carried out based on the 42 responses at the present time step and $m - 1$ previous time steps ($m = 4$ for this task). The collected current values were fed into a 168×1 software readout layer, which was trained through ridge regression, as shown in Fig. 6a. Following training in time steps 101 to 700, the testing results from time steps 701 to 1,000 were recorded and are shown in Fig. 6e, with a normalized root-mean-square error of 0.105, demonstrating that accurate prediction of MSO₃ time series can be achieved based on the multiple-timescale reservoir computing system.

Conclusions

We have reported a synaptic device that makes use of the ferroelectric and optoelectronic responses and tunable temporal dynamics of the α -In₂Se₃ semiconductor to enable multimode and multiscale signal processing. Short-term and long-term plasticity of the synapses was demonstrated, as well as excitatory and inhibitory functions such as PSC, PPF, PPD, LTP and LTD, using electrical and optical stimuli. Light or back-gate voltage can also be used as the modulation terminal to create heterosynaptic plasticity with tunable relaxation time and temporal dynamics. Based on the two distinct and tightly coupled physical processes in α -In₂Se₃, a reservoir computing system with adjustable nonlinear transformation was created for multimode signal processing. We also created a paralleled reservoir computer for multiscale signal processing, in which memristors with varied relaxation times are used to process different timescales. Due to the back-gate-tunable relaxation time and conductance range, multiscale features can be extracted, and accurate predictions made of the MSO₃ time series.

Methods

Material preparation and device fabrication

Single crystals of bulk α -In₂Se₃ were purchased from 2D Semiconductors (typical crystal size of ~ 8 mm and purity of $>99.9999\%$). Flakes of α -In₂Se₃ were mechanically exfoliated from a bulk single crystal and transferred onto a p-doped Si substrate covered with 10-nm-thick HfO₂ (Savannah, Cambridge NanoTech) grown by ALD. As a control experiment, flakes of MoS₂ were mechanically exfoliated from a bulk single crystal and transferred onto a p-doped Si substrate covered with

10-nm-thick ALD-grown HfO₂. The source and drain electrodes were patterned by electron-beam lithography (Raith Voyager), followed by electron-beam evaporation (typical thickness Au/Pd: 80 nm/5 nm) and liftoff processes to form the planar device with a source–drain distance of ~ 1 μ m.

Electrical measurements

Room-temperature electrical measurements were carried out using a Signatone probe station equipped with an Agilent B1500A semiconductor parameter analyser. A 655-nm laser was used in optoelectronic measurements; the power density of this was measured by a power meter (Newport 843-R). The low-temperature measurements were carried out in a Lakeshore cryogenic probe station in vacuum conditions, equipped with an Agilent B1500A semiconductor parameter analyser.

Material characterization

Raman spectra of the exfoliated α -In₂Se₃ flakes on the SiO₂ substrate were obtained using a Raman imaging microscope (Thermo Fisher Scientific DXRxi) with an excitation laser of 532 nm. Scanning electron microscopy (SEM) images and EDS element mapping of α -In₂Se₃ flakes as well as the cross-sectional TEM samples prepared by focused ion beam (FIB) were obtained using a dual-beam FIB system (FEI Helios NanoLab 600i) equipped with an EDS detector (Oxford X-Max^N 80). High-resolution STEM-HAADF images were obtained using a C_s-corrected TEM (FEI Titan Cubed Themis G2300) operated at 200 kV. The top-view TEM samples were prepared by transferring α -In₂Se₃ flakes onto holey carbon film supported on copper grids. HRTEM images were conducted using an FEI Tecnai F20 system operated at 200 kV. PFM measurements were performed using a multimode AFM device (Bruker Dimension Icon). Images were collected at contact resonance using a conductive tip with a spring constant of 3 N m⁻¹ and at non-contact resonance using a conductive tip with a spring constant of 80 N m⁻¹ to eliminate the electrostatic contribution.

Simulation

For the multimode handwritten digit-recognition task, the current responses were collected after every four pulses so that 100 current values were collected for each 20×20 digit. The readout layer was a 100×10 network, with ten outputs representing the ten different digits. The readout layer was realized in software, with 60,000 digits used for training and another 10,000 digits for testing. For the multimode QR code recognition task, the current responses were collected after every four pulses so that 200 current values were collected for each 40×20 QR code (0° and 90° with 25% noise). The readout layer was a 200×10 network, with ten outputs representing the ten different letters, and the readout layer was also realized in software. Three thousand QR codes with 25% noise were used for training, and another 1,000 QR codes with 25% noise were used for testing. A supervised algorithm, logistic regression, was utilized to train the readout networks for the multimode handwritten digit-recognition task and QR code recognition task. A sigmoid function was used as the activation function of the readout network to calculate the probability of different outputs. The cost function was minimized through the gradient descent method. For the MSO₃ task, the generated time series $u(t)$ and $-u(t)$ were linearly mapped to an appropriate voltage range (-1 V, -0.5 V), and the time interval between each time step was set as 20 ms. Two types of input ($u(t)$ and $-u(t)$) were applied to α -In₂Se₃ devices with varied back-gate voltages. The current values were then collected from the memristors with n types of back-gate voltages ($n = 21$), based on the response at the present time step and $m - 1$ previous time steps ($m = 4$). As a result, the collected current values were fed into a software readout with 168 input and 1 output, which was trained through ridge regression. The MSO₃ task consisted of 1,000 time steps, with time steps 1 to 100 used for washout, 101 to 700 for training and 701 to 1,000 for testing.

Data availability

The data that support the findings of this study are available on Zenodo (<https://zenodo.org/record/7120149#.YzRSL0xBw2w>). All other data are available from the corresponding author upon reasonable request.

Code availability

The codes used for simulation and data plotting are available from the corresponding authors upon reasonable request.

References

- Zheng, Z. et al. Unconventional ferroelectricity in moiré heterostructures. *Nature* **588**, 71–76 (2020).
- Fei, Z. et al. Ferroelectric switching of a two-dimensional metal. *Nature* **560**, 336–339 (2018).
- Chang, K. et al. Discovery of robust in-plane ferroelectricity in atomic-thick SnTe. *Science* **353**, 274–278 (2016).
- Higashitarumizu, N. et al. Purely in-plane ferroelectricity in monolayer SnS at room temperature. *Nat. Commun.* **11**, 2428 (2020).
- Yuan, S. et al. Room-temperature ferroelectricity in MoTe₂ down to the atomic monolayer limit. *Nat. Commun.* **10**, 1775 (2019).
- Si, M. W. et al. A ferroelectric semiconductor field-effect transistor. *Nat. Electron.* **2**, 580–586 (2019).
- Wang, S. et al. Two-dimensional ferroelectric channel transistors integrating ultra-fast memory and neural computing. *Nat. Commun.* **12**, 53 (2021).
- Wu, J. et al. High tunnelling electroresistance in a ferroelectric van der Waals heterojunction via giant barrier height modulation. *Nat. Electron.* **3**, 466–472 (2020).
- Wang, L. et al. Exploring ferroelectric switching in α -In₂Se₃ for neuromorphic computing. *Adv. Funct. Mater.* **30**, 2004609 (2020).
- Ding, W. et al. Prediction of intrinsic two-dimensional ferroelectrics in In₂Se₃ and other III₂-VI₃ van der Waals materials. *Nat. Commun.* **8**, 14956 (2017).
- Zhou, Y. et al. Out-of-plane piezoelectricity and ferroelectricity in layered α -In₂Se₃ nanoflakes. *Nano Lett.* **17**, 5508–5513 (2017).
- Xue, F. et al. Room-temperature ferroelectricity in hexagonally layered α -In₂Se₃ nanoflakes down to the monolayer limit. *Adv. Funct. Mater.* **28**, 1803738 (2018).
- Xue, F. et al. Gate-tunable and multidirection-switchable memristive phenomena in a van der Waals ferroelectric. *Adv. Mater.* **31**, 1901300 (2019).
- Gabel, M. & Gu, Y. Understanding microscopic operating mechanisms of a van der Waals planar ferroelectric memristor. *Adv. Funct. Mater.* **31**, 2009999 (2021).
- Si, M. et al. Asymmetric metal/ α -In₂Se₃/Si crossbar ferroelectric semiconductor junction. *ACS Nano* **15**, 5689–5695 (2021).
- Wan, S. et al. Nonvolatile ferroelectric memory effect in ultrathin α -In₂Se₃. *Adv. Funct. Mater.* **29**, 1808606 (2019).
- Xiao, J. et al. Intrinsic two-dimensional ferroelectricity with dipole locking. *Phys. Rev. Lett.* **120**, 227601 (2018).
- Cui, C. et al. Interrelated in-plane and out-of-plane ferroelectricity in ultrathin two-dimensional layered semiconductor In₂Se₃. *Nano Lett.* **18**, 1253–1258 (2018).
- Island, J. O., Blanter, S. I., Buscema, M., van der Zant, H. S. & Castellanos-Gomez, A. Gate controlled photocurrent generation mechanisms in high-gain In₂Se₃ phototransistors. *Nano Lett.* **15**, 7853–7858 (2015).
- Jacobs-Gedrim, R. B. et al. Extraordinary photoresponse in two-dimensional In₂Se₃ nanosheets. *ACS Nano* **8**, 514–521 (2014).
- Zhai, T. et al. Fabrication of high-quality In₂Se₃ nanowire arrays toward high-performance visible-light photodetectors. *ACS Nano* **4**, 1596–1602 (2010).
- Xue, F. et al. Optoelectronic ferroelectric domain-wall memories made from a single van der Waals ferroelectric. *Adv. Funct. Mater.* **30**, 2004206 (2020).
- Markovic, D., Mizrahi, A., Querlioz, D. & Grollier, J. Physics for neuromorphic computing. *Nat. Rev. Phys.* **2**, 499–510 (2020).
- Duan, Q. et al. Spiking neurons with spatiotemporal dynamics and gain modulation for monolithically integrated memristive neural networks. *Nat. Commun.* **11**, 3399 (2020).
- Zhou, F. et al. Optoelectronic resistive random access memory for neuromorphic vision sensors. *Nat. Nanotechnol.* **14**, 776–782 (2019).
- Yang, K. et al. Transiently chaotic simulated annealing based on intrinsic nonlinearity of memristors for efficient solution of optimization problems. *Sci. Adv.* **6**, eaba9901 (2020).
- Sebastian, A., Le Gallo, M., Khaddam-Aljameh, R. & Eleftheriou, E. Memory devices and applications for in-memory computing. *Nat. Nanotechnol.* **15**, 529–544 (2020).
- Liu, C. et al. Two-dimensional materials for next-generation computing technologies. *Nat. Nanotechnol.* **15**, 545–557 (2020).
- Zhu, J. et al. Ion gated synaptic transistors based on 2D van der Waals crystals with tunable diffusive dynamics. *Adv. Mater.* **30**, 1800195 (2018).
- Tuma, T., Pantazi, A., Le Gallo, M., Sebastian, A. & Eleftheriou, E. Stochastic phase-change neurons. *Nat. Nanotechnol.* **11**, 693–699 (2016).
- Yang, Y. & Huang, R. Probing memristive switching in nanoionic devices. *Nat. Electron.* **1**, 274–287 (2018).
- Li, C. et al. Analogue signal and image processing with large memristor crossbars. *Nat. Electron.* **1**, 52–59 (2018).
- Chen, S. et al. Wafer-scale integration of two-dimensional materials in high-density memristive crossbar arrays for artificial neural networks. *Nat. Electron.* **3**, 638–645 (2020).
- Jaeger, H. *The ‘Echo State’ Approach to Analysing and Training Recurrent Neural Networks—With an Erratum Note*. Technical Report GMD Report 148 (German National Research Center for Information Technology, 2001).
- Maass, W., Natschlager, T. & Markram, H. Real-time computing without stable states: a new framework for neural computation based on perturbations. *Neural Comput.* **14**, 2531–2560 (2002).
- Torrejon, J. et al. Neuromorphic computing with nanoscale spintronic oscillators. *Nature* **547**, 428–431 (2017).
- Moon, J. et al. Temporal data classification and forecasting using a memristor-based reservoir computing system. *Nat. Electron.* **2**, 480–487 (2019).
- Zhong, Y. et al. Dynamic memristor-based reservoir computing for high-efficiency temporal signal processing. *Nat. Commun.* **12**, 408 (2021).
- Du, C. et al. Reservoir computing using dynamic memristors for temporal information processing. *Nat. Commun.* **8**, 2204 (2017).
- Zhu, X., Wang, Q. & Lu, W. D. Memristor networks for real-time neural activity analysis. *Nat. Commun.* **11**, 2439 (2020).
- Sangwan, V. K. et al. Multi-terminal memtransistors from polycrystalline monolayer molybdenum disulfide. *Nature* **554**, 500–504 (2018).
- Wan, S. et al. Room-temperature ferroelectricity and a switchable diode effect in two-dimensional α -In₂Se₃ thin layers. *Nanoscale* **10**, 14885–14892 (2018).
- Liu, L. et al. Atomically resolving polymorphs and crystal structures of In₂Se₃. *Chem. Mater.* **31**, 10143–10149 (2019).
- Li, Y. et al. Orthogonal electric control of the out-of-plane field-effect in 2D ferroelectric α -In₂Se₃. *Adv. Electron. Mater.* **6**, 2000061 (2020).
- Xue, F. et al. Multidirection piezoelectricity in mono- and multilayered hexagonal α -In₂Se₃. *ACS Nano* **12**, 4976–4983 (2018).

46. Ho, C.-H. et al. Surface oxide effect on optical sensing and photoelectric conversion of α - In_2Se_3 hexagonal microplates. *ACS Appl. Mater. Interfaces* **5**, 2269–2277 (2013).
47. Wang, M. et al. Gesture recognition using a bioinspired learning architecture that integrates visual data with somatosensory data from stretchable sensors. *Nat. Electron.* **3**, 563–570 (2020).
48. Liu, M. et al. A star-nose-like tactile-olfactory bionic sensing array for robust object recognition in non-visual environments. *Nat. Commun.* **13**, 79 (2022).
49. Adelson, E. H., Anderson, C. H., Bergen, J. R., Burt, P. J. & Ogden, J. M. Pyramid methods in image processing. *RCA Eng.* **29**, 33–41 (1984).
50. Mozer, M. C. Induction of multiscale temporal structure. *Adv. Neural Inf. Process. Syst.* **4**, 275–282 (1992).
51. Hochreiter, S. & Schmidhuber, J. Long short-term memory. *Neural Comput.* **9**, 1735–1780 (1997).
52. Schmidhuber, J., Wierstra, D., Gagliolo, M. & Gomez, F. Training recurrent networks by Evolino. *Neural Comput.* **19**, 757–779 (2007).
53. Otte, S. et al. Optimizing recurrent reservoirs with neuro-evolution. *Neurocomputing* **192**, 128–138 (2016).

Acknowledgements

This work was supported by the National Key R&D Program of China (2017YFA0207600, to Y.Y.), the National Natural Science Foundation of China (61925401, to Y.Y.; 92064004, to Y.Y.; 61927901, to R.H.; 92164302, to Y.Y.), Project 2020BD010 was supported by the PKU-Baidu Fund and the 111 Project (B18001, to R.H.). Y.Y. acknowledges support from the Fok Ying-Tong Education Foundation and the Tencent Foundation through the XPLOER PRIZE. We acknowledge the Electron Microscopy Laboratory of Peking University, China for use of the C_s -corrected Titan Cubed Themis G2 300 transmission electron microscope.

Author contributions

K.L. and Y.Y. designed the experiments. K.L. and L.B. fabricated the devices. K.L. performed PFM measurements. K.L., L.X., C.C. and Z.Y.

performed electrical measurements. K.L. and T.Z. performed the simulations. K.L., B.D. and Y.Y. prepared the manuscript. Y.Y. and R.H. directed all the research and supervised the work. All authors analysed the results and implications and commented on the manuscript at all stages.

Competing interests

The authors declare no competing interests.

Additional information

Supplementary information The online version contains supplementary material available at <https://doi.org/10.1038/s41928-022-00847-2>.

Correspondence and requests for materials should be addressed to Ru Huang or Yuchao Yang.

Peer review information *Nature Electronics* thanks Matthew Dale, Matthew Marinella and the other, anonymous, reviewer(s) for their contribution to the peer review of this work.

Reprints and permissions information is available at www.nature.com/reprints.

Publisher's note Springer Nature remains neutral with regard to jurisdictional claims in published maps and institutional affiliations.

Springer Nature or its licensor holds exclusive rights to this article under a publishing agreement with the author(s) or other rightsholder(s); author self-archiving of the accepted manuscript version of this article is solely governed by the terms of such publishing agreement and applicable law.

© The Author(s), under exclusive licence to Springer Nature Limited 2022